

Anthropomorphic lung phantom based validation of in-room proton therapy 4D-CBCT image correction for dose calculation [☆]

David Bondesson ^{a,b,*}, Arturs Meijers ^c, Guillaume Janssens ^d, Simon Rit ^e, Moritz Rabe ^f, Florian Kamp ^f, Katharina Niepel ^g, Lydia A. den Otter ^c, Stefan Both ^c, Sebastien Brousmiche ^d, Julien Dinkel ^{a,b,h}, Claus Belka ^{f,i}, Katia Parodi ^g, Antje Knopf ^{c,j}, Christopher Kurz ^{f,g,1}, Guillaume Landry ^{f,g,*1}

^a Department of Radiology, University Hospital, LMU Munich, Munich, Germany

^b Comprehensive Pneumology Center (CPC-M), University Hospital, LMU Munich, Helmholtz Zentrum München, Member of the German Center for Lung Research (DZL), Munich, Germany

^c Department of Radiation Oncology, University Medical Center Groningen, University of Groningen, Groningen, The Netherlands

^d Advanced Technology Group, Ion Beam Applications SA Louvain-la-Neuve, Belgium

^e University of Lyon, CREATIS, CNRS UMR5220; Inserm U1044, INSA-Lyon, Université Lyon 1, Centre Léon Bérard, Lyon, France

^f Department of Radiation Oncology, University Hospital, LMU Munich, Munich, Germany

^g Department of Medical Physics, Faculty of Physics, Ludwig-Maximilians-Universität München (LMU Munich), Garching, Germany

^h Department of Radiology, Asklepios Lung Center Munich-Gauting, Germany

ⁱ German Cancer Consortium (DKTK), Munich, Germany

^j Division for Medical Radiation Physics, Carl von Ossietzky Universität Oldenburg, Germany

Received 29 May 2020; accepted 23 September 2020

Abstract

Purpose: Ventilation-induced tumour motion remains a challenge for the accuracy of proton therapy treatments in lung patients. We investigated the feasibility of using a 4D virtual CT (4D-vCT) approach based on deformable image registration (DIR) and motion-aware 4D CBCT reconstruction (MA-ROOSTER) to enable accurate daily proton dose calculation using a gantry-mounted CBCT scanner tailored to proton therapy.

Methods: Ventilation correlated data of 10 breathing phases were acquired from a porcine ex-vivo functional lung phantom using CT and CBCT. 4D-vCTs were generated by (1) DIR of the mid-position 4D-CT to the mid-position 4D-CBCT (reconstructed with the MA-ROOSTER) using a diffeomorphic Morphons algorithm and (2) subsequent propagation of the obtained mid-position vCT to the individual 4D-CBCT phases. Proton therapy treatment planning was performed to evaluate dose calculation accuracy of the 4D-vCTs. A robust treatment plan delivering a nominal dose of 60 Gy was generated on the average intensity image of the 4D-CT for an approximated internal target volume (ITV). Dose distributions were then recalculated on individual phases of the 4D-CT and the 4D-vCT based on the optimized plan.

Dose accumulation was performed for 4D-vCT and 4D-CT using DIR of each phase to the mid position, which was chosen as reference. Dose based on the 4D-vCT was then evaluated against the dose calculated on 4D-CT both, phase-by-phase as well as accumulated, by comparing dose volume histogram (DVH) values (D_{mean} , $D_{2\%}$, $D_{98\%}$, $D_{95\%}$) for the ITV, and by a 3D-gamma index analysis (global, 3%/3 mm, 5 Gy, 20 Gy and 30 Gy dose thresholds).

[☆] Wissenschaftspreis der DGMP 2018.

* Corresponding author: Guillaume Landry, Department of Radiation Oncology, University Hospital, LMU Munich, Munich, Germany.
E-mail addresses: david.bondesson@med.uni-muenchen.de (D. Bondesson), Guillaume.Landry@med.uni-muenchen.de (G. Landry).

¹ Equal contribution.

Results: Good agreement was found between the 4D-CT and 4D-vCT-based ITV-DVH curves. The relative differences ($(CT-vCT)/CT$) between accumulated values of ITV D_{mean} , $D_2\%$, $D_{95\%}$ and $D_{98\%}$ for the 4D-CT and 4D-vCT-based dose distributions were -0.2% , 0.0% , -0.1% and -0.1% , respectively. Phase specific values varied between -0.5% and 0.2% , -0.2% and 0.5% , -3.5% and 1.5% , and -5.7% and 2.3% . The relative difference of accumulated D_{mean} over the lungs was 2.3% and D_{mean} for the phases varied between -5.4% and 5.8% . The gamma pass-rates with 5 Gy, 20 Gy and 30 Gy thresholds for the accumulated doses were 96.7%, 99.6% and 99.9%, respectively. Phase-by-phase comparison yielded pass-rates between 86% and 97%, 88% and 98%, and 94% and 100%.

Conclusions: Feasibility of the suggested 4D-vCT workflow using proton therapy specific imaging equipment was shown. Results indicate the potential of the method to be applied for daily 4D proton dose estimation.

Keywords: Tomography, Cone-beam, Proton therapy, 4D-vCT, Motion, Thorax

1 Introduction

Ventilation-induced tissue motion remains a major challenge for accuracy in proton therapy of lung cancer, which is however deemed effective [1–3]. Optimal proton therapy treatment for lung cancer entails accounting for several sources of uncertainty, such as imaging artefacts (e.g. due to metal implants), organ motion, setup and anatomical variations and dose range uncertainties [4–8]. One of the challenges to precise treatment of lung cancer patients is ventilation motion, which can cause significant errors in imaging, patient alignment or, via interplay effects among others, in the delivered dose distribution [9]. These errors can lead to issues such as tumours not receiving the expected dose, or the heart (or other sensitive organs) receiving excessive radiation dose, having severe effects on both patient survival and complications [10]. To monitor and manage these issues, methods for monitoring and managing ventilation motion are being developed to create a treatment plan robustly optimized with respect to motion [11]. One important step has been to utilize a planning 4D-CT to establish a motion robust treatment plan. Complementing the planning CT, several studies have shown that CBCTs can yield further advantages by significantly reducing set-up errors and increasing radiotherapy (RT) accuracy [12–14]. Thus, daily on-board imaging and adaptive radiotherapy based on in-room 4D-cone beam CT (CBCT) has been suggested as an alternative [15]. However, to enable CBCT-based proton dose calculations for adaptation and/or plan re-optimization, accurate Hounsfield unit (HU) values are required [16,17]. To this end, correction strategies must be applied to CBCTs since their native image quality is severely degraded by, among others, scatter effects.

Also, 4D-CBCTs are not yet part of clinical proton therapy workflows since technical factors generally delayed CBCT's adoption compared to photon therapy [18]. Additionally, low image quality and thus poor soft tissue contrast have limited motion modelling. However, considerable progress has been made with novel motion-aware/-compensating image reconstruction methods [19–25]. These methods can be divided into ventilation-correlated or motion compensated approaches,

where the former may suffer from streaking artefacts due to a low number of projections in each reconstructed motion state and the latter only yields a static final image. To find a trade-off that would yield a more stable, yet still motion-aware reconstruction, a new method was recently introduced called motion-aware spatial and temporal regularization (MA-ROOSTER) [26]. It reconstructs a 4D-CBCT image from a motion averaged CBCT scan and the initial planning 4D-CT by performing spatial and temporal regularization, considering also that the voxel trajectories are curved based on the estimated ventilation motion of the 4D-CT. MA-ROOSTER has been shown to yield streak-free reconstructions and robust information on tumour location throughout the breathing cycle. Since direct accurate dose calculation on the obtained CBCT images is currently not feasible for proton therapy due to the previously mentioned downsides causing inaccurate HU values [27–29], it has instead been suggested to use the initial planning CT and the daily 4D-CBCT to generate a 4D-virtual CT (vCT) with the help of deformable image registration (DIR) [30–33]. The retrieved image will exhibit the anatomy and motion imaged by 4D-CBCT and contain the HU of the initial planning CT, such that accurate dose calculation can be performed [34–38]. This technique has been applied in the lungs by retrospectively sorting the CBCT images from a linac-mounted scanner into phases from extracted ventilation signals and performing phase-by-phase DIR [39]. However, the direct deformation of CT to CBCT phases for dosimetric evaluation means that each phase may suffer from CT to CBCT deformation uncertainties. In this work, we have investigated a novel mid position based vCT approach using the MA-ROOSTER workflow [40,41] and compared the dose calculation quality against planning 4D-CT for accumulated and phase-by-phase dosimetric evaluation. Measurements and evaluation were performed on a functional lung phantom using a proton-gantry-mounted CBCT system. In the presented workflow, only a single CT to CBCT DIR in mid position is used, followed by 3D-CBCT-to-4D-CBCT DIR to yield corrected CBCT images for each motion state, which should reduce uncertainties. To our knowledge, this is the first study to evaluate this novel 4D-vCT workflow using proton therapy specific imaging equipment.

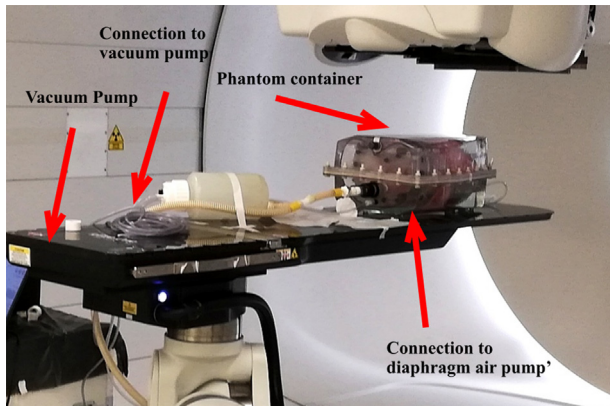


Figure 1. Ex vivo functional porcine lung phantom used for CBCT and CT measurements.

2 Materials and methods

2.1 Ex-vivo functional lung phantom

4D-CT and CBCT lung imaging was performed using a functional ex-vivo porcine lung phantom (Artichest[®], PROdesign GmbH, Heilkruststeinach, Germany) capable of executing user-defined breathing curves [42] (Fig. 1). The phantom is comprised of a water filled plastic shell which has a similar shape as a human thorax and contains inflatable porcine lungs. A thin layer of ultrasound gel was applied to the inside of the plastic shell, as well as onto the porcine lungs, to reduce friction between the plastic and lung surfaces. The lungs were then inflated by lowering the pressure inside the container with a constantly powered vacuum pump and the bronchi connected to outside pressure. A second pump was connected to a fabricated diaphragm layer, that cyclically changed its volume to simulate breathing motion. The breathing curve was defined manually to resemble a typical patient's breathing motion and was cyclically repeated with a frequency of 0.25 Hz (15 breaths per minute).

2.2 Image acquisition

2.2.1 4D-CT

A 4D-CT scan was acquired (Somatom Definition AS, Siemens Healthineers, Erlangen, Germany) covering the whole lung phantom during motion. The image set was sorted into 10 equidistant phase bins based on the diaphragm system pressure signal measured with an Anzai load cell (Anzai, Tokyo, Japan). The pressure sensor was connected via a T-pipe attached to the pressure input tube using a coupling adapter with an elastic membrane. The reconstruction grid was $0.977 \text{ mm} \times 0.977 \text{ mm} \times 2 \text{ mm}$ with 512×512 pixels per slice and 325 slices. CT images were reconstructed using an iterative reconstruction algorithm.

2.2.2 CBCT

The phantom was moved right after the CT acquisition to the treatment couch of a Proteus PLUS proton gantry (IBA, Louvain-la-Neuve, Belgium) for CBCT imaging. To ensure a reproducible ventilation cycle, the lung phantom was kept breathing with an uninterruptible power supply. The couch was equipped with a 6D robotic positioning system that was used to align the phantom to the treatment room's isocentre by using the on-board CBCT system. Images were acquired with an offset detector yielding a field of view of 50 cm diameter. The CBCT acquisition entailed the following parameters: rotation time 123s, source to image distance (SID)=3053.5 mm, source to axis distance (SAD)=2536 mm, tube voltage=120 kVp, exposure time=12.5 ms, tube current=320 mA, number of projections=910, gantry's angular range=359.23°.

2.3 Image reconstruction and generation

Reconstruction of 4D-CBCTs and 4D-vCT generation was performed with OpenReggii [43]. The 4D-CT and the CBCT projections were used as inputs to generate a 4D-CBCT and a mid position CBCT with the MA-ROOSTER workflow, as described below. These images were then used in the following step to generate the final 4D-vCT. For the purpose of presenting a clear overview, the workflow of the 4D-vCT reconstruction has been illustrated in Fig. 2. All DIRs were performed with an 8-level diffeomorphic Morphon algorithm [44]. The number of iterations between level 1 and 8 was set to 2/5/10/10/10/10/10/10 (finest to coarsest), similar to previous studies that performed CT-to-CBCT DIR [38].

2.3.1 MA-ROOSTER

MA-ROOSTER can be best understood as a general case of the initial 4D-ROOSTER algorithm [19] which in turn builds upon a 4D-conjugate gradient algorithm by adding temporal and spatial regularization terms. 4D-conjugate gradient (CG) aims to minimize the single-term cost function $\sum_{\alpha} \|R_{\alpha} S_{\alpha} f - p_{\alpha}\|_2^2$ where

1. $\|\cdot\|_2$ is the l_2 – norm.
2. α is the projection index.
3. f is a 4D-sequence of volumes to be reconstructed.
4. R_{α} is the forward projection operator at index α , mapping a 3D volume onto a 2D-projection image.
5. S_{α} is a linear interpolator that maps a 3D + time-sequence onto a 3D volume with the ventilation phase of projection α .
6. p_{α} is the measured projection with index α .

The ROOSTER algorithm adds regularization by considering the following constraints in every iteration:

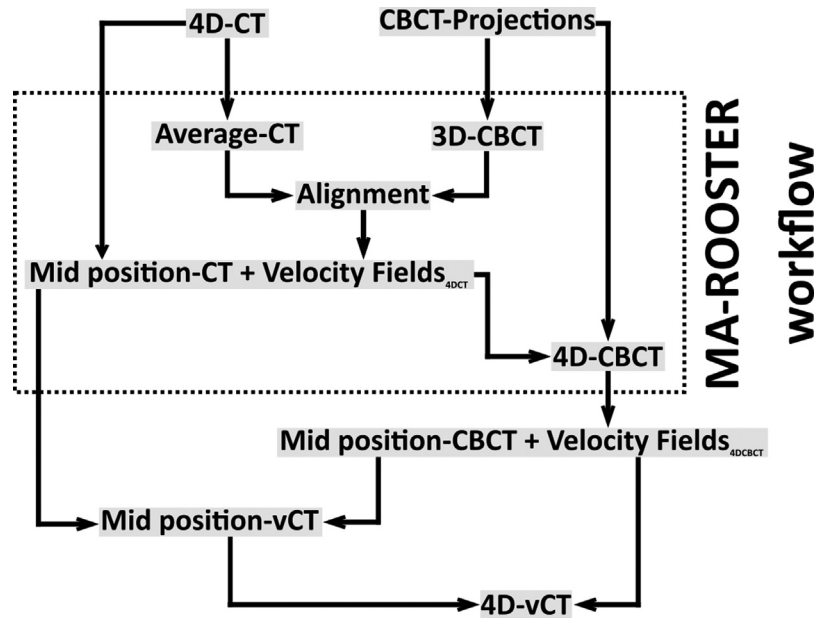


Figure 2. Workflow to generate a 4D-vCT image from a 4D-CT image and CBCT projections. MA-ROOSTER uses the CBCT projections to generate a 4D-CBCT. The initial planning 4D-CT is used to generate a mid position CT as well as to extract the DVFs input to the MA-ROOSTER.

- Minimize the single-term cost function $\sum_{\alpha} \|R_{\alpha} S_{\alpha} f - p_{\alpha}\|_2^2$ – with 4D-CG.
- Enforce positivity, by setting all negative voxels of f to zero.
- Remove motion where it is not expected to occur with a motion mask.
- Enforce the spatial and temporal gradients' sparsity in each volume using 3D- and 1D-total variation (TV) denoising along their respective dimensions [45].

It uses the output in every step as input for the next. However, as 1D-TV denoising is performed in the temporal direction by the ROOSTER method, moving objects in the lung have been observed to gradually fade from one position to another instead of displaying their actual sharp edges and a distinct position in every time frame. MA-ROOSTER tries to mitigate this specific problem by curving the regularization direction to follow moving structures. The MA-ROOSTER uses CBCT projections to generate a 3D-CBCT volume which, in turn, is used to extract a motion mask via segmentation to only include regions where motion is expected. The ventilation phase is usually extracted from the CBCT projections with the Amsterdam shroud method [46,47], but was ineffective with the lung phantom. It was instead extracted by tracking the areal change of a manually selected region in the CBCT projections that contained both lung and diaphragm. For extracting the motion that is used for curved regularization, deformation vector fields (DVF) [48] were generated from the 4D planning CT. The full MA-ROOSTER workflow is visualized inside the dotted box of Figure 2. The

implementation of the workflow can be summarized in the following steps:

- 1) The motion-averaged 3D-CBCT volume was reconstructed from the projections with the conjugate gradient descent method.
- 2) The motion mask was created from the blurry 3D-CBCT volume by segmenting the phantom (excluding surrounding air and the treatment couch).
- 3) The averaged 4D-CT was rigidly aligned to the 3D-CBCT with a mutual information metric and its rigid transformation was extracted.
- 4) A mid position CT and the corresponding 10 DVFs from each phase to mid position were generated following the steps described below. The DVFs were aligned to CBCT space with the rigid transformation.
- 5) The inverse of the DVFs from ventilation phases to mid position CT were used to generate the final 4D-CBCT in accordance with the MA-ROOSTER optimization steps described above.

The mid position CT and DVFs from ventilation phases to mid position were generated with the following steps:

- 1) DVFs from 9 phases to one reference phase were generated with DIR (see above for settings).
- 2) A mid position DVF was calculated by averaging the DVFs. All phases' DVFs are then subtracted from that to have them pointing towards the mid position.

- 3) The mid position image is then generated by deforming all images to mid position and calculating their median image.

The MA-ROOSTER workflow was performed using $359 \times 289 \times 270$ voxels on a $1 \text{ mm} \times 1 \text{ mm} \times 1 \text{ mm}$ grid. Regularization parameter γ_{space} and γ_{time} were set to 2×10^{-5} and 1×10^{-3} , respectively in accordance with the initial study's recommendation [26].

Since mismatching ventilation positions between the 4D planning CT and 4D-CBCT phases can cause anatomical differences [49], 9 incremental shifts of 1% (corresponding to 40ms) of the CBCT ventilation phase were performed on the extracted phase curve. 4D-CBCTs were reconstructed for every incremental shift and the breathing curves extracted by tracking the areal change in a manually selected region in the slices containing both lung and diaphragm. Correspondingly, the 4D-CT breathing curve was also extracted and compared against the extracted breathing curves with the smallest squared difference. This yielded an optimal incremental phase shift of 3% for matching 4D-CT and 4D-CBCT ventilation phases.

2.3.2 4D-vCT

The 4D-vCT generation uses the mid position CT and 4D-CBCT that were generated in the MA-ROOSTER workflow as inputs. Its workflow consists of the following steps:

- 1) A mid position CBCT phase was generated with the same multistep workflow described above to produce the mid position CT.
- 2) The mid position CT was non-rigidly registered onto the mid position CBCT (using the settings described above), generating a virtual mid position CT.
- 3) The mid position vCT was propagated to 4D with the extracted DVFs from the 4D-CBCT, yielding the 4D-vCT.

2.4 Treatment plan and dose optimization

Proton treatment plans were generated on a 3D average CT intensity image, obtained from voxel-wise averaging the 10 ventilation phases of the 4D-CT. A part of the oesophagus still attached to the lungs served as a surrogate gross tumour volume (GTV). An ITV was approximated by delineating this GTV with a narrow display (high contrast) window on the motion averaged CT image. The ITV was then copied onto each CT and vCT ventilation phase. The plan did not aim at reproducing treatment planning precisely, given the artificial nature of the simulated GTV. Rather, the goal was to generate reasonable dose distributions that could be used for recalculation and evaluation, and which covered the GTV at all ventilation phases. No density override was performed. Two pencil-beam scanning proton radiation fields at gantry angles 0° and 65° (on the International Electrotechnical Commission Scale) were planned to deliver 60 Gy in 30 fractions.

Dose calculation was performed with a pencil beam algorithm. Robust single field uniform dose optimization was performed for 21 scenarios with an isotropic position uncertainty of 5 mm and a range uncertainty of 3% using a research version of a commercial treatment planning system Raystation 6.99 (Raysearch Laboratories, Sweden) [50]. The optimized treatment plan was then recalculated on each phase of the 4D-CT and 4D-vCT.

2.5 Calculated accumulated dose

The generated diffeomorphic DVFs from phases to mid positions were used to subsequently deform and accumulate CT and vCT doses on their respective reference phase, similar to other recent dose accumulation studies [51,52]. The DVFs from the 4D-CBCT were used on the vCT doses, while the 4D-CT DVFs were used for the CT doses. The workflow for dose calculation and accumulation is further illustrated in Fig. 3.

Doses on CT and vCT were compared between phases as well as between the two accumulated results. DVH values (D_{mean} , $D_{2\%}$, $D_{95\%}$ and $D_{98\%}$) were calculated on the ITV as well as in the lungs not containing the ITV (D_{mean}). Cumulative DVH curves were obtained for the ITV as well as for the lungs excluding the ITV. 3D global gamma pass-rates were also calculated using a (3%, 3 mm) criterion and (total) dose thresholds of 5 Gy, 20 Gy and 30 Gy (corresponding to 8.3%, 33.3% and 50% of the prescribed dose).

3 Results

3.1 Comparison between registered CT and vCT

Fig. 4 displays sagittal slices of five exemplary ventilation phases of the 4D-CT, the reconstructed 4D-CBCT and the 4D-vCT images. The motion amplitude was estimated with the positional peak-to-peak change in the cranio-caudal direction of the diaphragm as well as the GTV, which showed to be 13 mm and 14 mm, respectively. Comparing the 4D-CT and 4D-vCT, a slight blurring was apparent on the latter due to interpolation. The bottom row displays the subtracted image of the 4D-CT and 4D-vCT, illustrating anatomical differences caused by the 4D-vCT generation algorithm. The difference images highlight a phase-dependent misalignment at the edges of the diaphragm position, particularly visible in phases 2 and 6 (red arrows). However, this area was far from the simulated treatment area in our study and subject to substantial sliding tissue motion due to the construction of the phantom.

3.2 Accumulated dose CT and vCT

The difference in dose distribution between the 4D-CT and 4D-vCT is depicted in Fig. 5 for ventilation phases 2, 4, 6, 8 and 10. The figure highlights that doses within the 50% threshold region differ by less than 0.3 Gy (compared to the 2 Gy fraction dose). Larger dose differences were observed in the

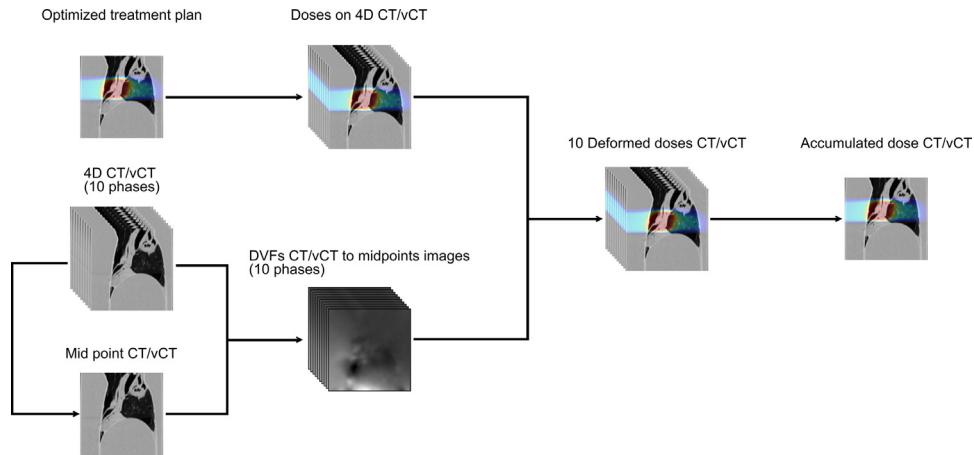


Figure 3. Workflow to calculate the accumulated dose for both 4D-CT and 4D-vCT. The optimized treatment plan was generated on the averaged intensity image of the 4D-CT. The treatment plan (upper left corner) was optimized on a voxel-wise image averaged along the 10 ventilation phases.

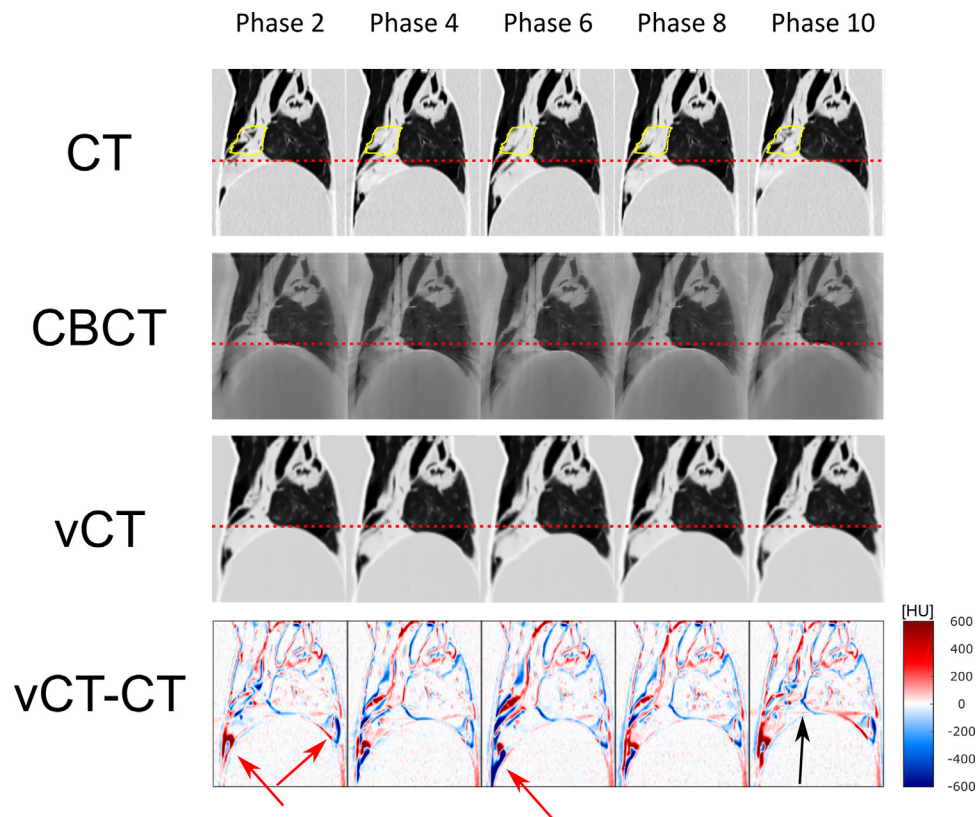


Figure 4. (1st to 3rd row) Display of sagittal slices from 4D-CT as well as reconstructed 4D-CBCT and 4D-vCT images (ventilation phases 2, 4, 6, 8 and 10). Dotted lines highlight the diaphragm position at maximum exhale. The ITV is depicted in yellow. (4th row) Sagittal slices of difference images (4D vCT minus 4D-CT) in HU. Red arrows highlight particular registration discrepancies occurring particularly around transitional points between tissue and the phantom. The black arrow highlights a vertical registration discrepancy at the same height as streaking artefacts produced in the CBCT reconstructions.

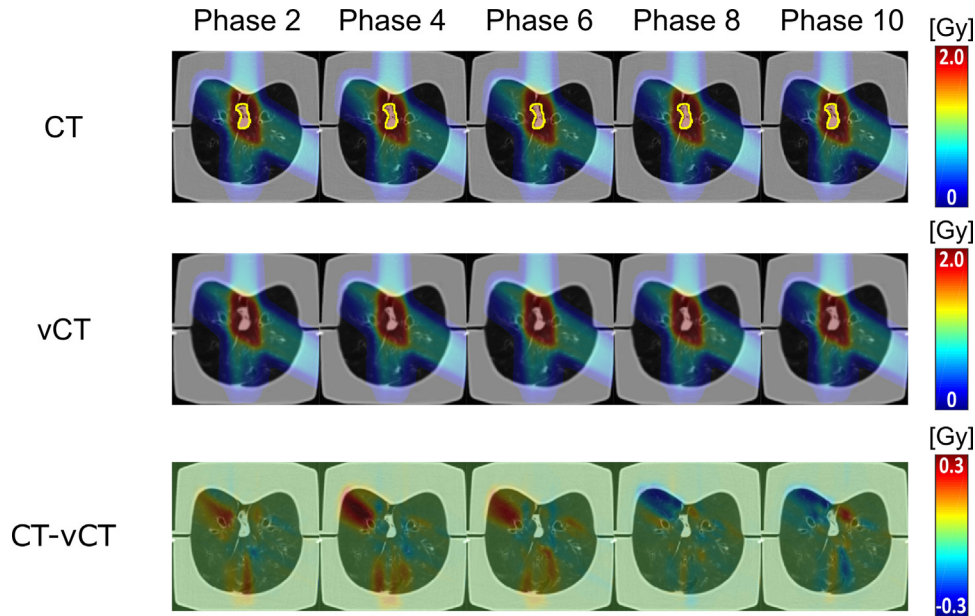


Figure 5. Dose distributions (top and middle row) and dose differences (bottom row) on phases 2, 4, 6, 8 and 10 between 4D-CT and 4D-vCT images. The ITV is displayed on the 4D-CT in yellow.

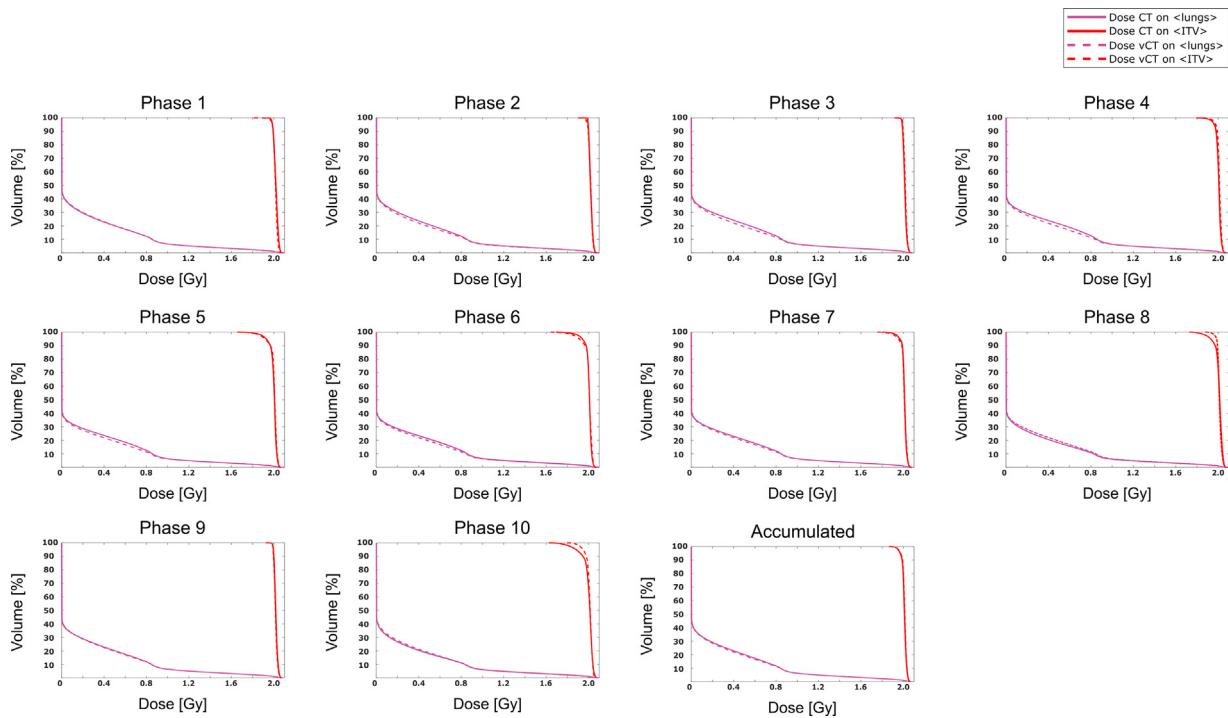


Figure 6. Comparison of DVH curves for the ITV and lungs (without the ITV) from 4D-vCT (solid) and 4D-CT (dotted) doses (all phases and accumulated).

distal, low dose areas, of each field, where range differences expand given the low lung density. Gamma index pass-rates for the accumulated dose distributions between 4D-CT and 4D-vCT were 96.7%, 99.6% and 99.9% respectively for the

5 Gy, 20 Gy and 30 Gy thresholds, respectively. Table 1 further displays the gamma pass-rates for all single-phase dose recalculations, ranging from 85.5% to 95.2%, 88.4% to 98.0% and 97.6% to 99.9% for the three considered thresholds. The

Table 1
Gamma pass-rates (PR) calculated for a global 3%/3 mm passing criteria and different dose thresholds.

	PR 5 Gy threshold [%]	PR 20 Gy threshold [%]	PR 30 Gy threshold [%]
Phase 1	97.4	98.0	97.6
Phase 2	89.3	94.8	98.3
Phase 3	85.5	91.3	99.7
Phase 4	87.7	88.4	99.9
Phase 5	87.6	90.4	99.8
Phase 6	91.5	93.3	99.7
Phase 7	95.2	96.8	99.9
Phase 8	92.4	95.9	94.4
Phase 9	95.7	97.5	99.7
Phase 10	95.2	96.7	94.1
Accumulated	96.7	99.6	99.9

DVHs (Fig. 6) confirm the good agreement between CT and vCT based dose for both the ITV and lungs excluding the ITV, with worst performance for phases 8 and 10. Table 2 shows the quantitative DVH comparison results between 4D-CT and 4D-vCT for all ventilation phases and the accumulated doses. Discrepancies for the ITV were found to be within 5.7% for the single phases and within 0.2% for the accumulated dose. Discrepancies for the phase-by-phase evaluation in the lungs without the ITV were found to be within 5.8% and within 2.3% for the accumulated dose.

4 Discussion

In this work we have generated 4D-vCTs using diffeomorphic mid position CT to mid position CBCT DIR and the MA-ROOSTER workflow for calculating the accumulated proton dose in a porcine lung phantom. For the comparison of the accumulated doses on 4D-CT and 4D-vCT, gamma pass-rates of 96.7%, 99.6% and 99.9% were determined for 5 Gy, 20 Gy and 30 Gy dose thresholds (prescribed total dose was 60 Gy). Considering also the observed discrepancies of

only -0.1% for D_{mean} , 0.0% for $D_{2\%}$, -0.2% for $D_{95\%}$ and -0.1% for $D_{98\%}$ of the ITV, the feasibility to deform the planning 4D-CT into a 4D-vCT with updated motion, to be used for daily 4D proton dose estimation, can be concluded. The motion amplitudes (peak-to-peak) for the lung phantom's diaphragm and the GTV in this study were 13 mm and 14 mm showing a good correspondence with clinically observed values [53]. For the phase-resolved evaluation, the largest DVH differences on the ITV were observed in phases 8 and 10, which also had the lowest pass-rates for the 30 Gy threshold gamma analysis. The lower the used dose threshold was in the gamma evaluation, the lower pass-rates were yielded. This is probably due to the low density of the lung in the lower dose region, where small errors in the 4D-vCT can translate into large range shifts. Comparing reconstructed vCT images against the reference CT for the respective phases, registration artefacts are found, as shown in Fig. 4 (red arrows), at the anterior side of the lungs. This is particularly visible when observing the transitional points between tissue and the phantom diaphragm where the DVF in phase 2 has caused a slight bend in diaphragm and outer shell shape. Furthermore, streaking artefacts from the CBCT reconstruction have been observed in several phases but were particularly visible in phase 10 (black arrow in Fig. 4). Regularization parameters can be manually adapted to remedy this effect, however, it is conceptually challenging to model substantial tissue motion while maintaining diffeomorphic properties of the DVFs [26]. Still, it should be noticed that the artefacts were far from the treatment field in our study. However, this could cause issues for dosimetric calculations of irradiated tumours positioned in the lower parts of the lung. It should, nevertheless, also be considered that the anatomy of the phantom is not entirely realistic in the lower part of the lung due to the excessive sliding motion, which would likely not appear to such extent in a real patient. Blurring was visible in all reconstructed images, but the good agreement of dose distributions suggests that it likely only has a negligible effect. Furthermore, compared to previous similar attempts to perform dose evaluation on

Table 2
(2nd to 4th column) Differences $((\text{CT}-\text{vCT})/\text{CT})$ in $D_{2\%}$, $D_{95\%}$, $D_{98\%}$ and D_{mean} between dose calculations on 4D-CT and 4D-vCT for the ITV. (5th column) D_{mean} differences between dose calculations on 4D-CT and 4D-vCT for the lungs (without the ITV). Values are displayed for all ventilation phases as well as for the accumulated dose from all 10 phases.

	$\Delta D_{2\%}(\text{ITV})$ [%]	$\Delta D_{95\%}(\text{ITV})$ [%]	$\Delta D_{98\%}(\text{ITV})$ [%]	$\Delta D_{\text{mean}}(\text{ITV})$ [%]	$\Delta D_{\text{mean}}(\text{lungs})$ [%]
Phase 1	0.4	0.1	0.3	0.2	-0.4
Phase 2	0.1	0.3	0.7	0.1	5.1
Phase 3	-0.1	-0.2	-0.3	-0.2	5.5
Phase 4	-0.1	-0.7	-0.9	-0.3	5.8
Phase 5	-0.1	0.6	1.1	-0.1	5.1
Phase 6	-0.2	1.5	2.3	0.1	4.3
Phase 7	-0.1	0.7	1.2	0.1	3.2
Phase 8	0.1	-2.8	-4.9	-0.25	-5.4
Phase 9	0.1	0.1	0.0	0.1	1.1
Phase 10	0.5	-3.5	-5.7	-0.5	1.5
Accumulated	-0.0	-0.2	-0.1	-0.1	2.3

4D-vCT phases from photon radiotherapy CBCT systems with phase-by-phase CT to CBCT DIR all gamma pass-rates and dose differences were comparable or improved [39].

Establishing a precise daily 4D motion model with the patient in treatment position is essential for tracking tumour motion since it may enable adaptive dose planning. This in turn could be used to optimize coverage of dose to the target while sparing essential organs-at-risk during radiation therapy treatment. The presented 4D-vCT workflow adapts the necessary balance between stable and motion-aware reconstruction by using the novel MA-ROOSTER method and enables accurate estimation of the accumulated and phase-specific dose compared to the 4D planning CT. This may subsequently improve estimation of the accumulated dose between treatments and adaptation of the total treatment plan accordingly. The conjugate gradient descent method for the initial 3D-CBCT reconstruction ensures that regularization can be utilized to decrease movement artefacts compared to the analytical Feldkamp, Davis and Kress reconstruction [54,55]. Additionally, the MA-ROOSTER has shown to yield a good agreement with daily motion as well as attenuation properties when DVFs from CT and CBCT differ strongly [26], highlighting the 4D-vCT workflow's generality also for differing ventilation trajectories. Also, since the focus of this study was mainly on dosimetric evaluation of the 4D-vCT workflow, investigation of the impact of inconsistent ventilation trajectories in 4D-CT and 4D-CBCT was considered out of scope.

There are some limitations to this study besides the use of the same motion between the 4D-CT and the 4D-CBCT scans. Since measurements were performed on a porcine lung phantom this should be seen as a proof of principle study. Future studies with patient measurements and larger sample sizes are required to establish further clinical relevance. For example, to compare the presented dose comparison workflow between an initial planning 4D-CT and a CBCT with differing tumour size would be of particular interest. On the other hand, investigating clinical patient data typically lacks ground truth information, since breathing motion is not reproducible between 4D-CT and 4D-CBCT acquisitions. The used pencil beam algorithm for dose calculation in lieu of a Monte Carlo algorithm may have yielded less precise dose estimates, particularly in the low dose heterogeneous regions of the lung [56]. However, since a single algorithm was consistently used for optimization and recalculation, we deem that the performed dosimetric analysis allows for reliable estimation of the accuracy achievable with the presented 4DvCT approach.

Furthermore, as the workflow requires approximately 50 min performing the reconstructions with multiple registration steps, it needs further improvements before it can be implemented into online clinical application. The workflow currently performs image reconstruction both on the GPU and CPU and faster reconstruction could potentially be reached if all parts would run on the GPU.

5 Conclusion

In this work, a porcine lung phantom was used to show that the suggested 4D-vCT reconstruction workflow for CBCT intensity correction is feasible using proton therapy specific imaging equipment. A dosimetric evaluation using a 4D-CT exhibiting the same motion as the 4D-CBCT shows promise for the method to be used for daily 4D-proton dose estimation. Comparison between 4D-vCT and 4D-CT showed discrepancies for ITV D_{mean} , $D_{2\%}$, $D_{95\%}$ and $D_{98\%}$ within 0.2%. Global 3%/3 gamma pass-rates for the accumulated doses were above 96.7% for dose thresholds of 5 Gy, 20 Gy and 30 Gy. A more detailed evaluation, also encompassing 4D-CT and 4D-CBCT data with different motion trajectories was deemed beyond the scope of this proof-of-principle study but might be addressed in follow-up studies.

Conflict of interests

The authors declare that they have no known competing financial interests or personal relationships that could have appeared to influence the work reported in this paper.

Acknowledgements

This work was supported by the German Research Foundation (DFG) project 399148265 “4D cone beam computed tomography as a novel tool for accurate time-resolved dose calculation in particle therapy”, the DFG's Cluster of Excellence Munich-Centre for Advanced Photonics (MAP) and the DFG Research Training Group GRK2274 Advanced Medical Physics for Image-Guided Cancer Therapy.

References

- [1] Chen J, Lu JJ, Ma N, Zhao J, Chen C, Fan M, et al. Early stage non-small cell lung cancer treated with pencil beam scanning particle therapy: retrospective analysis of early results on safety and efficacy. *Radiat Oncol* 2019;14:16.
- [2] Nakajima K, Iwata H, Ogino H, Hattori Y, Hashimoto S, Toshito T, et al. Clinical outcomes of image-guided proton therapy for histologically confirmed stage I non-small cell lung cancer. *Radiat Oncol* 2018;13:199.
- [3] Ono T, Nakamura T, Yamaguchi H, Azami Y, Takayama K, Suzuki M, et al. Clinical results of proton beam therapy for elderly patients with non-small cell lung cancer. *Radiat Oncol* 2018;13:19.
- [4] Knopf A-C, Lomax A. In vivo proton range verification: a review. *Phys Med Biol* 2013;58:R131–60.
- [5] Yang M, Zhu XR, Park PC, Titt U, Mohan R, Virshup G, et al. Comprehensive analysis of proton range uncertainties related to patient stopping-power-ratio estimation using the stoichiometric calibration. *Phys Med Biol* 2012;57:4095–115.
- [6] Paganetti H. Range uncertainties in proton therapy and the role of Monte Carlo simulations. *Phys Med Biol* 2012;57:R99–117.
- [7] Chen M, Yang J, Liao Z, Chen J, Xu C, He X, et al. Anatomic change over the course of treatment for non-small cell lung cancer patients and its impact on intensity-modulated radiation therapy and passive-scattering proton therapy deliveries. *Radiat Oncol* 2020;15:55.

- [8] Baumann K-S, Flatten V, Weber U, Lautenschläger S, Eberle F, Zink K, et al. Effects of the Bragg peak degradation due to lung tissue in proton therapy of lung cancer patients. *Radiat Oncol* 2019;14:183.
- [9] Zhang Y, Yin F-F, Ren L. Dosimetric verification of lung cancer treatment using the CBCTs estimated from limited-angle on-board projections. *Med Phys* 2015;42:4783–95.
- [10] Chun SG, Solberg TD, Grosshans DR, Nguyen Q-N, Simone CBI, Mohan R, et al. The potential of heavy-ion therapy to improve outcomes for locally advanced non-small cell lung cancer. *Front Oncol* 2017;7.
- [11] Gomez DR, Chang JY. Adaptive radiation for lung cancer. *J Oncol* 2011, <http://dx.doi.org/10.1155/2011/898391>.
- [12] Borst GR, Sonke J-J, Betgen A, Remeijer P, Herk van M, Lebesque JV. Kilo-voltage cone-beam computed tomography setup measurements for lung cancer patients; first clinical results and comparison with electronic portal-imaging device. *Int J Radiat Oncol Biol Phys* 2007;68:555–61.
- [13] Grills IS, Hugo G, Kestin LL, Galerani AP, Chao KK, Wloch J, et al. Image-guided radiotherapy via daily online cone-beam CTx substantially reduces margin requirements for stereotactic lung radiotherapy. *Int J Radiat Oncol Biol Phys* 2008;70:1045–56.
- [14] Bissonnette J-P, Purdie TG, Higgins JA, Li W, Bezjak A. Cone-beam computed tomographic image guidance for lung cancer radiation therapy. *Int J Radiat Oncol Biol Phys* 2009;73:927–34.
- [15] Harsolia A, Hugo GD, Kestin LL, Grills IS, Yan D. Dosimetric advantages of four-dimensional adaptive image-guided radiotherapy for lung tumors using online cone-beam computed tomography. *Int J Radiat Oncol* 2008;70:582–9.
- [16] Yoo S, Yin F-F. Dosimetric feasibility of cone-beam CT-based treatment planning compared to CT-based treatment planning. *Int J Radiat Oncol Biol Phys* 2006;66:1553–61.
- [17] Hatton J, McCurdy B, Greer PB. Cone beam computerized tomography: the effect of calibration of the Hounsfield unit number to electron density on dose calculation accuracy for adaptive radiation therapy. *Phys Med Biol* 2009;54:N329–46.
- [18] Landry G, Hua C. Current state and future applications of radiological image guidance for particle therapy. *Med Phys* 2018;45:e1086–95.
- [19] Mory C, Auvray V, Zhang B, Grass M, Schäfer D, Chen SJ, et al. Cardiac C-arm computed tomography using a 3D+ time ROI reconstruction method with spatial and temporal regularization. *Med Phys* 2014;41:021903.
- [20] Sonke J-J, Zijp L, Remeijer P, Herk van M. Respiratory correlated cone beam CT. *Med Phys* 2005;32:1176–86.
- [21] Ritschl L, Sawall S, Knaup M, Hess A, Kachelrieß M. Iterative 4D cardiac micro-CT image reconstruction using an adaptive spatio-temporal sparsity prior. *Phys Med Biol* 2012;57:1517–25.
- [22] Wu H, Maier A, Fährig R, Hornegger J. Spatial-temporal total variation regularization (STTVR) for 4D-CT reconstruction. *Med Imaging 2012 Phys Med Imaging International Society for Optics and Photonics* 2012:83133J.
- [23] Wang J, Gu X. Simultaneous motion estimation and image reconstruction (SMEIR) for 4D cone-beam CT. *Med Phys* 2013;40:101912.
- [24] Brehm M, Paysan P, Oelhafen M, Kunz P, Kachelrieß M. Self-adapting cyclic registration for motion-compensated cone-beam CT in image-guided radiation therapy. *Med Phys* 2012;39:7603–18.
- [25] Liu J, Zhang X, Zhang X, Zhao H, Gao Y, Thomas D, et al. 5D respiratory motion model based image reconstruction algorithm for 4D cone-beam computed tomography. *Inverse Probl* 2015;31:115007.
- [26] Mory C, Janssens G, Rit S. Motion-aware temporal regularization for improved 4D cone-beam computed tomography. *Phys Med Biol* 2016;61:6856–77.
- [27] Kurz C, Dedes G, Resch A, Reiner M, Ganswindt U, Nijhuis R, et al. Comparing cone-beam CT intensity correction methods for dose recalculation in adaptive intensity-modulated photon and proton therapy for head and neck cancer. *Acta Oncol* 2015;54:1651–7.
- [28] Fotina I, Hopfgartner J, Stock M, Steininger T, Lütgendorf-Caucig C, Georg D. Feasibility of CBCT-based dose calculation: comparative analysis of HU adjustment techniques. *Radiother Oncol J Eur Soc Ther Radiol Oncol* 2012;104:249–56.
- [29] Siewerdsen JH, Jaffray DA. Cone-beam computed tomography with a flat-panel imager: magnitude and effects of X-ray scatter. *Med Phys* 2001;28:220–31.
- [30] Peroni M, Ciardo D, Spadea MF, Riboldi M, Comi S, Alterio D, et al. Automatic segmentation and online virtualCT in head-and-neck adaptive radiation therapy. *Int J Radiat Oncol Biol Phys* 2012;84:e427–33.
- [31] Veiga C, McClelland J, Moinuddin S, Lourenço A, Ricketts K, Annkah J, et al. Toward adaptive radiotherapy for head and neck patients: feasibility study on using CT-to-CBCT deformable registration for “dose of the day” calculations. *Med Phys* 2014;41:031703.
- [32] Wu Q, Chi Y, Chen PY, Krauss DJ, Yan D, Martínez A. Adaptive replanning strategies accounting for shrinkage in head and neck IMRT. *Int J Radiat Oncol Biol Phys* 2009;75:924–32.
- [33] Zhang T, Chi Y, Meldolesi E, Yan D. Automatic delineation of on-line head-and-neck computed tomography images: toward on-line adaptive radiotherapy. *Int J Radiat Oncol Biol Phys* 2007;68:522–30.
- [34] Landry G, Dedes G, Zöllner C, Handrack J, Janssens G, Xivry de JO, et al. Phantom based evaluation of CT to CBCT image registration for proton therapy dose recalculation. *Phys Med Biol* 2014;60:595–613.
- [35] Landry G, Nijhuis R, Dedes G, Handrack J, Thieke C, Janssens G, et al. Investigating CT to CBCT image registration for head and neck proton therapy as a tool for daily dose recalculation. *Med Phys* 2015;42:1354–66.
- [36] Thomson DJ, Teo B-KK, Ong A, Ang KW, Kirk M, Ahn PH, et al. The impact of anatomic change on pencil beam scanning in the treatment of oropharynx cancer. *Int J Part Ther* 2015;2:394–403.
- [37] Veiga C, Alshaikhi J, Amos R, Lourenço AM, Modat M, Ourselin S, et al. Cone-beam computed tomography and deformable registration-based “dose of the day” calculations for adaptive proton therapy. *Int J Part Ther* 2015;2:404–14.
- [38] Veiga C, Janssens G, Teng C-L, Baudier T, Hotoiu L, McClelland JR, et al. First clinical investigation of cone beam computed tomography and deformable registration for adaptive proton therapy for lung cancer. *Int J Radiat Oncol Biol Phys* 2016;95:549–59.
- [39] Niepel K, Kamp F, Kurz C, Hansen D, Rit S, Neppel S, et al. Feasibility of 4DCBCT-based proton dose calculation: an ex vivo porcine lung phantom study. *Z Für Med Phys* 2019;29:249–61.
- [40] Wolthaus JWH, Sonke J-J, Herk van M, Damen EMF. Reconstruction of a time-averaged midposition CT scan for radiotherapy planning of lung cancer patients using deformable registration. *Med Phys* 2008;35:3998–4011.
- [41] Wanet M, Sterpin E, Janssens G, Delor A, Lee JA, Geets X. Validation of the mid-position strategy for lung tumors in helical TomoTherapy. *Radiother Oncol* 2014;110:529–37.
- [42] Biederer J, Dinkel J, Remmert G, Jetter S, Nill S, Moser T, et al. 4D-Imaging of the lung: reproducibility of lesion size and displacement on helical CT MRI, and cone beam CT in a ventilated ex vivo system. *Int J Radiat Oncol Biol Phys* 2009;73:919–26.
- [43] openREGGUI consortium. Image processing open-source platform for adaptive proton therapy in cancer treatment; 2016. <https://openreggui.org/>.
- [44] Janssens G, Jacques L, Orban de Xivry J, Geets X, Macq B. Diffeomorphic registration of images with variable contrast enhancement. *Int J Biomed Imaging* 2011:2011.
- [45] Jacques L, Hammond DK, Fadili JM. Dequantizing compressed sensing: when oversampling and non-Gaussian constraints combine. *IEEE Trans Inf Theory* 2011;57:559–71.
- [46] Zijp L, Sonke JJ, Van Herk MB. Extraction of the respiratory signal from sequential thorax cone-beam X-ray images. *Proc 14th ICCR Seoul, Korea* 2004:507–9.
- [47] Van Herk MB, Zijp L, Remeijer P, Wolthaus J, Sonke JJ. On-line 4D cone beam CT for daily correction of lung tumour position during hypofractionated radiotherapy. *Proc 15th ICCR Toronto, Canada* 2007.

- [48] Dang J, Luo O, Gu X, Wang J. Deformation vector fields (DVF)-driven image reconstruction for 4D-CBCT. *J X-ray Sci Technol* 2015;23:11–23.
- [49] Dietrich L, Jetter S, Tücking T, Nill S, Oelfke U. Linac-integrated 4D cone beam CT: first experimental results. *Phys Med Biol* 2006;51:2939–52.
- [50] Bodensteiner D. RayStation: external beam treatment planning system. *Med Dosim* 2018;43:168–76.
- [51] Kurz C, Maspero M, Savenije MHF, Landry G, Kamp F, Pinto M, et al. CBCT correction using a cycle-consistent generative adversarial network and unpaired training to enable photon and proton dose calculation. *Phys Med Biol* 2019;64:225004.
- [52] Meijers A, Jakobi A, Stützer K, Marmitt GG, Both S, Langendijk JA, et al. Log file-based dose reconstruction and accumulation for 4D adaptive pencil beam scanned proton therapy in a clinical treatment planning system: implementation and proof-of-concept. *Med Phys* 2019;46:1140–9.
- [53] Rit S, van Herk M, Zijp L, Sonke J-J. Quantification of the variability of diaphragm motion and implications for treatment margin construction. *Int J Radiat Oncol Biol Phys* 2012;82:e399–407.
- [54] Pengpan T, Smith ND, Qiu W, Yao A, Mitchell CN, Soleimani M. A motion-compensated cone-beam CT using electrical impedance tomography imaging. *Physiol Meas* 2010;32:19–34.
- [55] Rit S, Sarrut D, Desbat L. Comparison of analytic and algebraic methods for motion-compensated cone-beam CT reconstruction of the thorax. *IEEE Trans Med Imaging* 2009;28:1513–25.
- [56] Grassberger C, Daartz J, Dowdell S, Ruggieri T, Sharp G, Paganetti H. Quantification of proton dose calculation accuracy in the lung. *Int J Radiat Oncol* 2014;89:424–30.

Available online at www.sciencedirect.com

ScienceDirect